Geophys. J. Int. (2008) **173,** 1106–1118 doi: 10.1111/j.1365-246X.2008.03777.x

Lithosphere of the Dharwar craton by joint inversion of *P* and *S* receiver functions

S. Kiselev,[1] L. Vinnik,[1] S. Oreshin,[1] S. Gupta,[2] S. S. Rai,[2] A. Singh,[2] M. R. Kumar[2] and G. Mohan[3]

[1] *Institute of Physics of the Earth, B. Grouzinskaya* 10, 123995 *Moscow, Russia. E-mail: vinnik@ifz.ru*
[2] *National Geophysical Research Institute, Hyderabad*-500 007, *India*
[3] *Department of Earth Sciences, Indian Institute of Technology, Powai, Mumbai* 400076, *India*

Accepted 2008 March 2. Received 2008 February 18; in original form 2007 March 22

SUMMARY

The Archean Dharwar craton in south India is known for long time to be different from most other cratons. Specifically, at station Hyderabad (HYB) the *Ps* converted phases from the 410- and 660-km mantle discontinuities arrive up to 2 s later than in other cratons of comparable age, which implies lower upper mantle velocities. To resolve the unique lithosphere–asthenosphere system of the Dharwar craton, we inverted jointly *P* and *S* receiver functions and teleseismic *P* and *S* traveltime residuals at 10 seismograph stations. This method operates in the same depth range as long-period surface waves but differs by much higher lateral and radial resolution. We observe striking differences in crustal structures between the eastern and western Dharwar craton (EDC and WDC, respectively): crustal thickness is of around 31 km, with predominantly felsic velocities, in the EDC and of around 55 km, with predominantly mafic velocities, in the WDC. In the mantle we observe significant variations in the *P* velocity with depth, practically without accompanying variations in the *S* velocity. In the mantle *S* velocity there are azimuth-dependent indications of the Hales discontinuity at a depth of ∼100 km. The most conspicuous feature of our models is the lack of the high velocity mantle keel with the *S* velocity of ∼4.7 km s^{-1}, typical of other Archean cratons. The *S* velocity in our models is close to 4.5 km s^{-1} from the Moho to a depth of ∼250 km. There are indications of a similar upper mantle structure in the northeast of the Indian craton and of a partial recovery of the normal shield structure in the northwest. A division between the high *S*-velocity western Tibet and low *S*-velocity eastern Tibet may be related to a similar division between the northeastern and northwestern Indian craton.

Key words: Composition of the mantle; Body waves; Wave propagation; Cratons; Crustal structure; Asia.

1 INTRODUCTION

The Indian craton is amalgamation of a few smaller cratons (Drury *et al.* 1984; Taylor *et al.* 1984). Its southern part is occupied by the Dharwar craton (Fig. 1). The mid-Archean greenstone belt in the western Dharwar craton (WDC) presents one of the oldest cratonic nuclei (Raase *et al.* 1986). Evolution of the greenstone belt is a consequence of volcanism around 3.6 Gyr ago and stabilization at 2.7 Gyr. In the north, the WDC is covered by 65 Myr old Deccan traps (DVP, Deccan Volcanic Province). The late Archean granite–gneiss terrain of the eastern Dharwar craton (EDC) was formed at 2.5 Gyr and stabilized in early Proterozoic. The southernmost Dharwar craton is occupied by the Southern Granulite Terrain (SGT).

The Dharwar craton differs in the properties of the upper mantle from most other cratons of comparable age. The difference is suggested by the observations of the *P*-to-*S* (*Ps*) converted phases from the discontinuities bounding the mantle transition zone (TZ) at around 410–660 km depths. Topography on the discontinuities can be significant in anomalously hot and cold regions of the TZ—hotspots and subduction zones, respectively—but in other regions the arrival times of the *Ps* converted phases are controlled mainly by the wave velocities in the crust and mantle over the 410 km discontinuity (Chevrot *et al.* 1999). We use IASP91 standard earth model (Kennett & Engdahl 1991) as a reference. At seismograph stations in the Archean cratons (Canadian, Siberian, East-European, Kalahari in southern Africa and some others), the *Ps* converted phases from the TZ discontinuities arrive up to 2 s earlier than in IASP91 (Chevrot *et al.* 1999); early arrivals are caused by the high *S* velocities in the roots of the cratons, extending to a depth of about 250 km. However, the arrivals of $P_{410}s$ and $P_{660}s$ at seismograph station Hyderabad (HYB) in south India (Fig. 1) are observed practically at the standard time (Chevrot *et al.* 1999). A similar time is observed at stations in the DVP (Kumar & Mohan 2005).

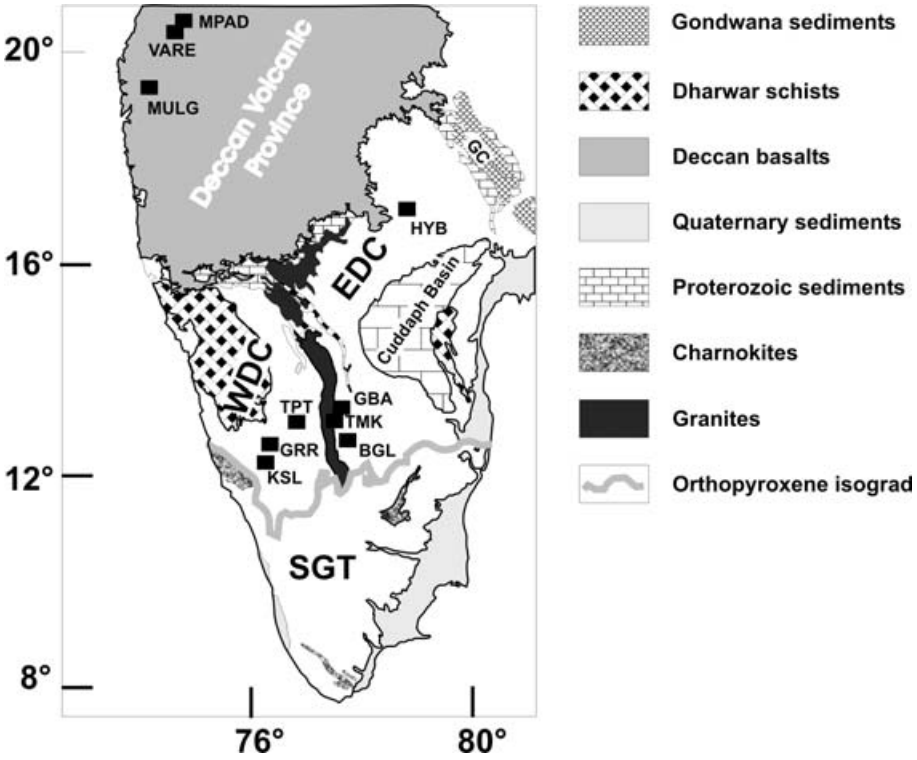

Figure 1. Tectonic map of south India with seismograph stations.

There are two alternative upper-mantle models that may account for these observations. In the first model, the velocities are close to those in IASP91 in the whole depth range from the Moho to the 410-km discontinuity. In the second model, the high *S*-velocity (around 4.7 km s^{-1}) mantle keel of the craton is present only at shallow depths (less than about 150 km), but at the larger depths it is replaced by a low-velocity layer (*S* velocity around 4.3 km s^{-1}), perhaps related to a hot mantle plume. The bottom part of the keel might be lost during the rapid drift of the Indian plate in the Mesozoic. Negi *et al.* (1986) advocated the model with a thin high-velocity lithosphere and a pronounced low *S*-velocity layer which would explain super-mobility of the Indian lithosphere in the Mesozoic.

To be understood, the unique lithosphere–asthenosphere system of the Indian shield requires a detailed characterization by seismic means. In the past it was explored by a number of seismological techniques (e.g. Bhattacharya 1992; Kaila & Krishna 1992; Gaur & Priestley 1997; Mohan *et al.* 1997; Zhou *et al.* 2000; Kumar *et al.* 2001; Sarkar *et al.* 2001; Gupta *et al.* 2003; Rai *et al.* 2003; Krishna 2004; Ramesh *et al.* 2005; Mitra *et al.* 2006), which include controlled source seismology, *P* receiver functions and surface waves. These observations require inversion for a velocity model which is non-unique. Moreover, the results of different studies are often not complementary owing to large differences in scales and resolution. Several crustal studies were based on *P* receiver functions at very short periods (around 1 s), where the recordings are severely contaminated by random wave scattering. The available mantle *S*-velocity models are obtained from observations of long period surface waves. Dharwar craton in these studies is sometimes indistinguishable from the neighbouring ocean.

Here, to image the crust and mantle beneath the Dharwar craton to a depth of 250–300 km, we use new seismic techniques. The idea is to invert jointly *P* and *S* receiver functions (PRFs and SRFs, respectively) and teleseismic *P* and *S* traveltime residuals. PRFs contain transmitted *Ps* (converted from *P* to *S*) phases, but reflected and scattered seismic phases from shallow discontinuities, which arrive at the same time, can be easily mistaken for the *Ps* phases from deep discontinuities. In the SRFs, the *Sp* (converted from *S* to *P*) phases from deep discontinuities arrive much earlier than the reflected phases from shallow discontinuities. PRFs and SRFs are complementary (comparable in lateral resolution but different in radial resolution at different depths) and their joint inversion reduces non-uniqueness of each method (Vinnik *et al.* 2004). The non-uniqueness of inversion can be further reduced by a joint inversion of the receiver functions and the absolute (determined with respect to the known velocity model) teleseismic *P* and *S* traveltime residuals (Vinnik *et al.* 2006). In general, our method operates in the same depth range as long-period surface waves (from the Earth surface to a depth of 250–300 km) but differs by much higher lateral and radial resolution.

2 METHODS

The PRFs and SRFs present a response of the Earth's medium in the vicinity of the seismograph station to excitation by teleseismic *P* (for the PRF) or *S* waves (for the SRF). This response includes either *Ps* (in the PRF) or *Sp* (in the SRF) converted phases.

To construct the PRFs, we applied the technique (Vinnik 1977), in which a 3-component seismogram is projected on the axes *L* and *Q*. Axis *L* is parallel to the principal *P* wave particle motion direction in the wave propagation plane. The angle i_P between *L* and the vertical direction, can be found from the related covariance matrix. Axis *Q* is normal to *L* in the same plane and is nearly optimum for observing the *Ps* converted phases. Both components of each recording are deconvolved by the *L* component. Deconvolution is performed in

time domain (Berkhout 1977) with a proper regularization (damping parameter is equal to 3.0).

To detect the *Ps* phases from deep discontinuities, the individual *Q* components are stacked with move-out time corrections. Like in Vinnik (1977) and other similar studies, the adopted reference slowness is 6.4 s/° (seconds per degree). The result of stacking is presented as a set of traces for different trial conversion depths. The depth of the discontinuity can be found accurately from the arrival time of the *Ps* converted phase, or it can be evaluated tentatively as a trial conversion depth corresponding to the largest amplitude of this phase. A compatibility of both estimates implies that an arrival is identified correctly as the *Ps* phase.

Calculation of the SRF (Farra & Vinnik 2000) involves seismogram decomposition into *Q*, *L*, *T* and *M* components. The *Q* and *L* components here are different from those in the PRFs. *Q* corresponds to the principal *S* particle motion direction in the wave propagation plane. Angle i_{SV} between the *Q* axis and the radial direction is determined from the related covariance matrix. *L* is perpendicular to *Q* in the same plane and is nearly optimum for detecting the *Sp* converted phases. *T* is perpendicular to the wave propagation plane, and *M* is the principal *S* particle motion component in the plane containing the *Q* and *T* components. The angle θ between the axes *Q* and *M* is controlled by the focal mechanism of the earthquake. All components are deconvolved by the *M* component.

The *Sp* converted phases can be generated by the *SV* and *SH* (in the case of azimuthal anisotropy) components of the incoming *S* wave. To isolate the *Sp* phases generated by *SV*, the individual receiver functions of many events are stacked with weights depending on θ and the level of noise. The result of stacking is the *L* component deconvolved by the *Q* component of the *S* wave and normalized to the amplitude of the *Q* component. The procedure involves evaluation of σ, the rms value of noise in the stack. To account for the difference in slowness between the *S* and *Sp* phases from deep discontinuities, the individual receiver functions are stacked with time corrections (slant stacking). The correction is calculated as the product of the trial differential slowness and the differential epicentral distance (difference between the epicentral distance of the seismic event and the reference epicentral distance of the group of events). The stack is calculated for a number of values of the differential slowness. The move-out corrections for different depths of conversion can be calculated more accurately, but at the relatively long periods of the SRFs (around 10 s) and in the narrow range of the *S* wave slowness (between 12.3 s $(^\circ)^{-1}$ at a distance of 65° and 9.2 s $(^\circ)^{-1}$ at a distance of 90°) the gain in accuracy is negligible.

The SRF technique is most efficient in the distance range between 65° and 90°. In the distance range between 75° and 90°, *SKS* seismic phase arrives within 30 s of *S*, and at around 83°, they even arrive at the same time. How the potential interference between *S* and *SKS* affects performance of the SRF technique? The *Sp* and *SKSp* converted phases from discontinuities at depths less than 100 km arrive with a negligible difference in time (small relative to the dominant period of 10 s), but at larger depth the difference becomes significant, around 10 s for a depth of 400 km. The 410-km discontinuity is global, and the converted phases from this discontinuity are of great diagnostic value. Numerical simulations reveal three possible kinds of interaction between *S* and *SKS* in *S* receiver functions: (1) contribution of *SKS* to the wave train used is small relative to *S*; (2) contribution of *S* is small relative to *SKS* and (3) contributions of *S* and *SKS* are comparable. In the first case, the detected signal is $S_{410}p$, in the 2nd case this is $SKS_{410}p$. In the 3rd case, no signal is detected because the waveform used for deconvolution is strongly different from both *S* and *SKS*. We will show that in most of our receiver functions, the detected signal is $S_{410}p$ with implication that the *S* wave is dominant and the effect of interference between *S* and *SKS* is small.

Constraining the models by the teleseismic traveltime residuals (Vinnik *et al.* 2006) is based on the fact that the major mantle discontinuities are related to the phase transitions, the depths of which depend on the temperature. Outside the anomalously hot and cold regions (hotspots and subduction zones, respectively), the difference between the arrival times of the $P_{660}s$ and $P_{410}s$ phases (23.9 s) is stable, with implications that the discontinuities are located virtually at the same depths (Chevrot *et al.* 1999). Then the lateral variations of times of these phases are controlled by the *P* and *S* velocities at depths less than 410 km. The arrival time of the *Ps* converted phase is measured relative to the *P* wave. Therefore, the anomaly of the arrival time of the *Ps* phase $\mathrm{d}T_{Ps}$ can be presented as $\mathrm{d}T_{Ps} = \mathrm{d}T_S - \mathrm{d}T_P$, where $\mathrm{d}T_S$ and $\mathrm{d}T_P$ are the absolute teleseismic traveltime residuals of the *S* and *P* waves, respectively. Following Vinnik *et al.* (1999) this relation can be written as $\mathrm{d}T_P = \mathrm{d}T_{Ps}/(k-1)$; $\mathrm{d}T_S = \mathrm{d}T_{Ps}\,[1 + 1/(k-1)]$, where *k* is the ratio between the *S* and *P* residuals. For the same length of the wave path for the *P* and *S* waves, and assuming that the velocity variations are caused by the temperature, $k = 2.7$ (Vinnik *et al.* 1999). In the PRFs, the wave path of the *S* wave is shorter than of the *P* wave by ∼ 10 per cent. With the correction for the difference in lengths of the wave paths, $k = 2.4$. We assume, in agreement with numerous studies (e.g. Grand 2002), that the largest lateral *P* and *S* velocity variations are in the upper 250–300 km of the Earth, in the layer sampled by the receiver functions. Then the *P* and *S* residuals thus obtained, $\mathrm{d}T_P$ and $\mathrm{d}T_S$ can be used to constrain the velocity profiles inferred from the receiver functions.

Our technology of inversion of the receiver functions was previously described by Vinnik *et al.* (2006, 2007). Nevertheless, for the convenience of the reader we describe it again. We assume that the Earth in the vicinity of the station is homogeneous and isotropic. As a rule, we use the 0 km trace of the PRFs and 0 s/° trace of SRFs. Other traces could be more appropriate for depths around 200 km, but at the relatively long periods of our receiver functions this effect is negligible. The model is defined by the *P* and *S* velocities V_P and V_S, density and thickness of each plane layer. Density is derived from the *P* velocity by using Birch law. For the PRFs and SRFs we calculate synthetic *Q* and *L* components, respectively, as:

$$Q_{P,\mathrm{syn}}(t, \mathbf{m}, cp) = \frac{1}{2\pi}\int_{-\infty}^{+\infty} \frac{H_{P,Q}(\omega, \mathbf{m}, cp)}{H_{P,L}(\omega, \mathbf{m}, cp)} \times L_{P,\mathrm{obs}}(\omega)\exp(i\omega t)\,\mathrm{d}\omega, \quad (1)$$

$$L_{SV,\mathrm{syn}}(t, \mathbf{m}, cs) = \frac{1}{2\pi}\int_{-\infty}^{+\infty} \frac{H_{SV,L}(\omega, \mathbf{m}, cs)}{H_{SV,Q}(\omega, \mathbf{m}, cs)} \times Q_{SV,\mathrm{obs}}(\omega)\exp(i\omega t)\,\mathrm{d}\omega. \quad (2)$$

Here *t* is time, ω is angular frequency, $\mathbf{m}$ is the vector of unknown model parameters, c_P and c_S are the adopted apparent velocities for the PRFs and SRFs, respectively, indices 'obs' and 'syn' correspond to the actual receiver functions and their synthetic analogues, respectively, and *H* are theoretical transfer functions for the stack of plane layers. Angles i_P and i_{SV} are known for each individual receiver function but not for the stacked ones. Also, sometimes the calculated receiver functions are later additionally filtered without changing the angles i_P and i_{SV} . Therefore, in the inversion these angles are included in $\mathbf{m}$ and allowed to vary within a few degrees

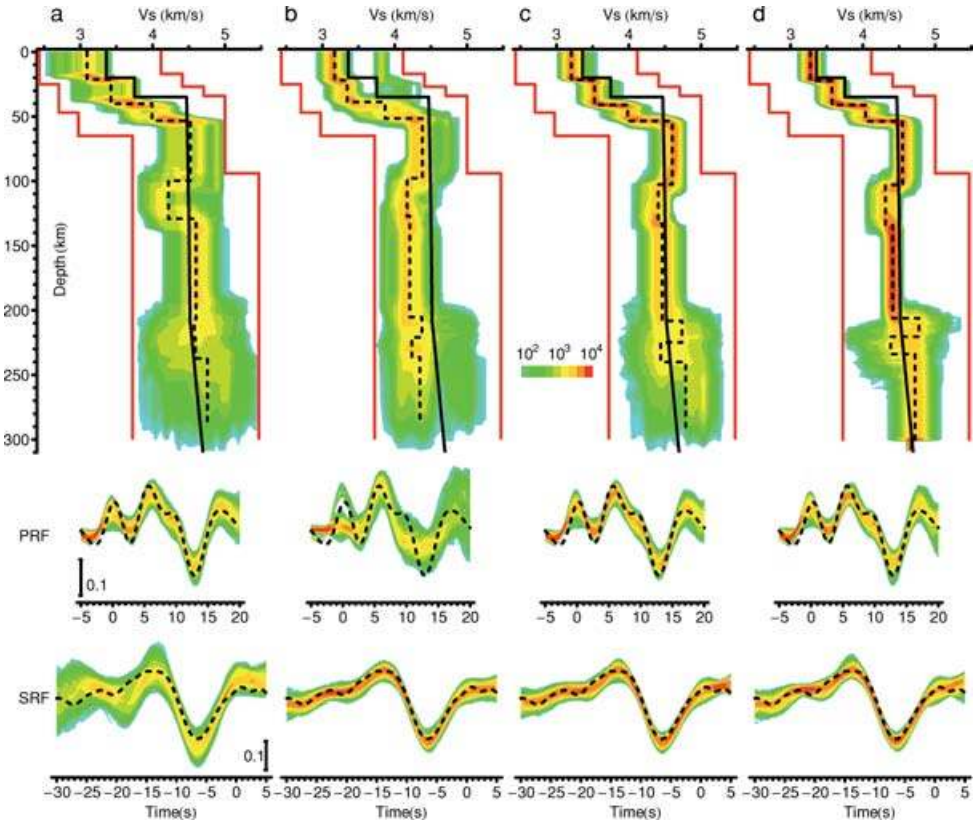

Figure 2. Histograms of the *S* velocity (colour code) obtained by inversion of the PRFs (a), SRFs (b), PRFs and SRFs (c), PRFs, SRFs and the *P* and *S* traveltime residuals (d) from station CHAT in the Tien Shan (modified from Vinnik *et al.* 2006). IASP91 velocities and medians are shown by bold and dash lines, respectively. The related synthetic *Q* components of the PRFs and the *L* components of the SRFs are shown with the same colour code; the actual components are shown by dash lines.

of their respective average values. The values of c_P and c_S are fixed at the average values of apparent velocities for the *P* and *S* waves, respectively. The synthetic receiver functions are calculated with the aid of Thomson–Haskell matrix algorithm (Haskell 1962). Earth flattening transformation is applied as in Biswas (1972).

Let E_P (**m**) and E_S (**m**) be misfits for the stacked *Q* components of the PRFs and *L* components of the SRFs, respectively. The misfit (cost) is defined as the rms difference between the observed and synthetic functions. The inversion is then to manipulate **m** to minimize E_P (**m**) and E_S (**m**) simultaneously. We conduct a search for the optimum models by using an interactive algorithm, similar to Simulated Annealing (Mosegaard & Vestergaard 1991): the cost functions are minimized by applying a set of moves, that is, a set of model perturbations, and accepting or rejecting the moves according to the Metropolis rule (Metropolis *et al.* 1953). For the two cost functions we use the Metropolis rule in cascade (Mosegaard & Tarantola 1995).

The Metropolis rule is formulated by using a parameter termed temperature. We use step-wise temperature function. The value of temperature at each step is chosen by the condition that the search, when initialized at an arbitrary point $\mathbf{m}_0$ within chosen bounds, converges to the same point for any $\mathbf{m}_0$. The inversion procedure may require several temperature iterations. For a new iteration we set narrowed bounds resulting from the previous iteration, and repeat manual adjustment of temperature. The procedure is terminated when the cost function in the convergence point has reached sufficiently small pre-defined level, usually around 0.02. To visualize the results of the inversion we divide the parameter space into cells, and present the models by the number of hits in each cell, and show this number by the colour code. A similar statistics is demonstrated for the data space.

The technique for the joint inversion of the PRF and SRF (using the Metropolis rule in cascade for the two functions) can be easily extended for the joint inversion of the receiver functions and the traveltime residuals. The traveltime residuals for the trial models are evaluated by ray tracing in the spherical Earth for the average apparent velocities of the *P* receiver functions.

Advantages of the joint inversion are illustrated by the data from station CHAT in the Tien Shan (Fig. 2, modified from Vinnik *et al.* 2006) and from station HYB of the present study (Fig. 3). For each station, we show the histograms of the *S* velocity obtained by the inversion of only the PRF (a), only the SRF (b), both PRF and SRF (c), and PRF, SRF and the traveltime residuals (d). We also show the histograms of the related synthetic PRFs and SRFs. At station CHAT, the models in (a) are not optimal for the SRF; this is expressed in a large scatter of the synthetic SRFs. Similarly, the models in (b) are not optimal for the PRFs. The joint inversion (c) yields the models that are optimal for both the PRF and the SRF. Finally, the histogram of the *S* velocity from the PRF, SRF and the traveltime residuals (d) is more narrow than the others, and some details of the models are more clear—a high velocity mantle lid and the underlying LVZ with a boundary between them at a depth around 100 km. The LVZ is terminated at a depth of 200–230 km (the Lehmann discontinuity).

Qualitatively similar effects of the joint inversion are evident in the data from station HYB (Fig. 3). The histogram of the *S* velocity

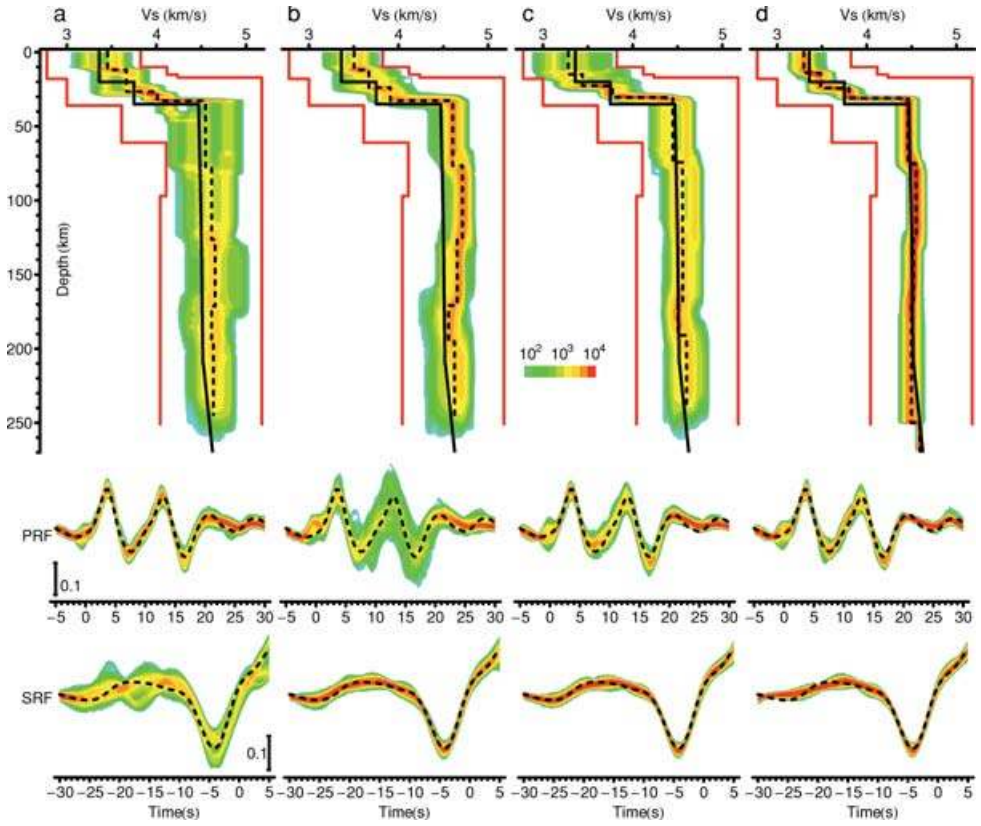

Figure 3. The same as Fig. 2, but from station HYB of the present study.

in (d) is very narrow and reveals a weak but distinct positive discontinuity (with a higher velocity at the lower side) at a depth around 80 km. The crustal histogram is narrow in (d) relative to (c) in spite of the fact that the traveltime residuals are accumulated mainly in the mantle. However, the model velocities in the crust and the mantle depend on each other via the receiver functions and constraining the velocities in the mantle affects those in the crust.

In the last years, the SRF techniques were practiced by several groups of researchers (e.g. Angus *et al.* 2006; Wilson *et al.* 2006). The most important distinctions of our methodology are, first, the rigorous inversion technique, and second, the joint inversion of the SRFs, PRFs and the traveltime residuals. In most studies, the SRFs are transformed into the velocity models semi-intuitively, and the positive bump between −10 and −20 s in Figs 2 and 3 is interpreted as the *Sp* phase from the 'LAB', the boundary between the high velocity mantle lid and the underlying LVZ. In reality the stacked *Q* component, which is practically never shown in the published papers, may contain in addition to the main lobe, two smaller side-lobes with opposite polarities (Fig. 4), and the *Sp* phases should have about the same wave forms. The bump is either the side-lobe of the *Sp* phase from the Moho or a result of interference of the side-lobes and the main lobes of a few *Sp* phases. The solution is impossible without a rigorous inversion technique.

3 DATA AND RESULTS

We use recordings of 10 seismograph stations within the Dharwar craton (Fig. 1). Station HYB in the EDC belongs to the Geoscope network and provides a large number of useful recordings. Other stations belong to local networks, which operated usually less than 2 yr. This time span is generally too short for obtaining a sufficiently large number (on the order of several tens) of the SRFs. To have a

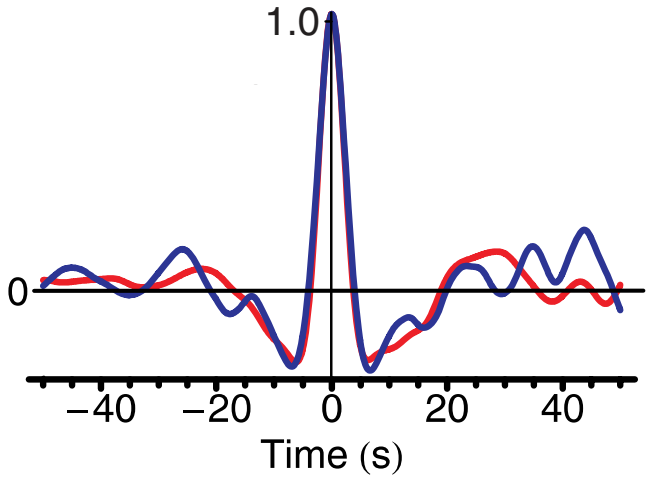

Figure 4. Stacked *Q* components of the SRFs from stations CHAT (blue) and HYB (red).

high signal-to-noise ratio in the stack of the SRFs, we combined the data of the closely spaced stations GBA, BGL and TMK in the EDC into a single data set, termed EDC. In the previous studies (Gupta *et al.* 2003) the crust beneath these stations was found laterally homogeneous, to the first approximation. For the same reasons, the data of stations GRR, TPT and KSL (Gupta *et al.* 2003) in the WDC are combined in the other set, termed WDC. The data of stations MULG, MPAD and VARE (Kumar & Mohan 2005) in the DVP are also combined into a single set, termed DVP.

Most SRFs are obtained at epicentral distances between 65° and 90°. The distance range for the PRFs is from 40° to 90°. The azimuth

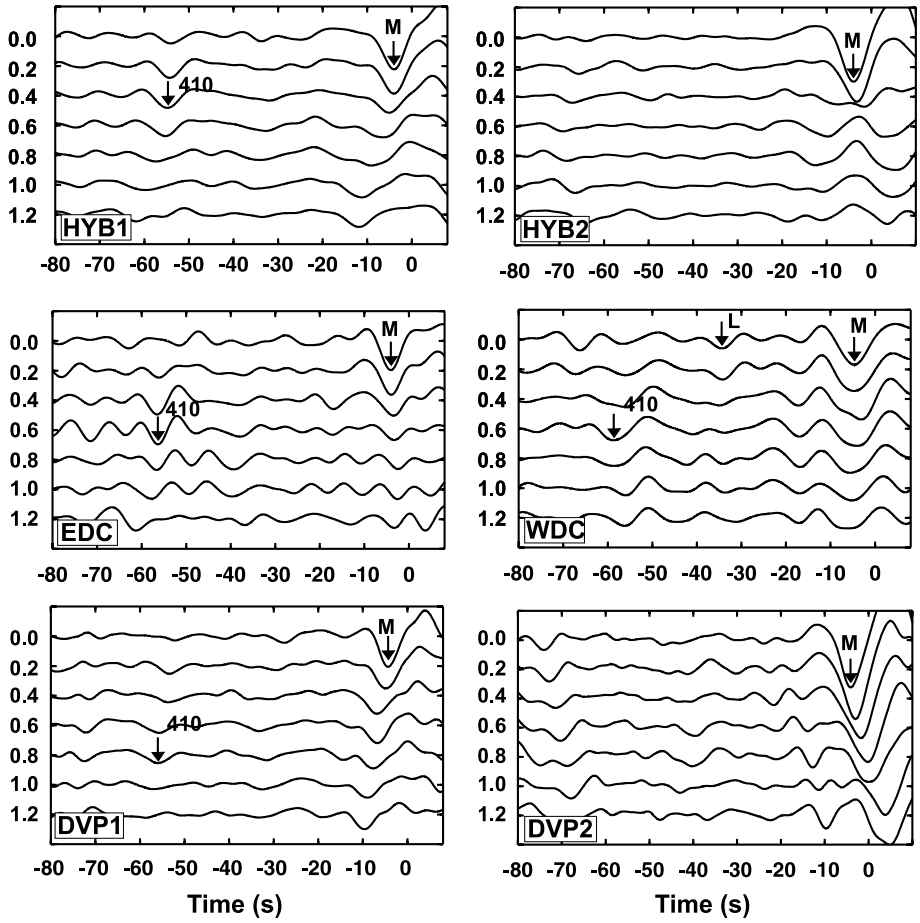

Figure 5. Stacked L components of the SRFs from station HYB in the backazimuths of about 100° ('HYB1') and 40° ('HYB2'); GBA + BGL + TMK in the backazimuth of about 100° ('EDC'); GRR + TPT + KSL in the backazimuths of about 100° ('WDC'); MULG + MPAD + VARE in the backazimuths of about 100° (DVP1) and 40° (DVP2). Each trace corresponds to the differential slowness in s/°, shown on the left-hand side. Origin of the timescale corresponds to the arrival of the *S* wave train, but *S* waves are not seen. Arrivals of the $S_{410}p$ phase are labeled 410 at the traces with the largest amplitude. The arrival labeled *M* at the 0.0 s/° trace is formed by the *Sp* phases from the Moho and other crustal discontinuities. The arrival labeled *L* is the *Sp* phase presumably from the Lehmann discontinuity.

around 100° yields many good *S* wave recordings and it is well represented in the data from all stations. Another backazimuth sector, with most azimuths between 30° and 50° and the average around 40° is represented only in the recordings from HYB and DVP. The data from the first azimuth are labelled HYB1 and DVP1, and those from the second azimuth are HYB2 and DVP2.

For HYB1, we stacked 55 individual SRFs with the average epicentral distance of 77°. Standard error (rms value of noise in the stack) is 0.009. For the adopted sign convention, negative polarity of the *Sp* phase corresponds to positive discontinuity (with a higher *S* velocity at the lower side). Beyond the *Sp* phase from the Moho at a time of −4.2 s, the stack contains a clear $S_{410}p$ phase at a time around −55 s with the largest amplitude (around 0.05) at 0.4 s $(^\circ)^{-1}$. (Fig. 5). This differential slowness is close to the theoretical value of 0.6 s $(^\circ)^{-1}$. For HYB2, we stacked 69 individual SRF3 with the average epicentral distance of 77.2° and the rms value of noise of 0.009. The only clear signal in this stack is the *Sp* phase from the Moho.

For EDC, we stacked 26 SRFs with the average epicentral distance of 76° and the rms value of noise of 0.013. This stack contains the clear *Sp* phase from the Moho at a time of −4.2 s and the $S_{410}p$ phase with the maximum amplitude at a differential slowness of 0.6 s $(^\circ)^{-1}$. For WDC we stacked 67 SRFs, the rms value of noise is 0.009. Both major *Sp* phases (from the Moho and 410 km discontinuity) are present, the latter at a differential slowness of 0.6 s $(^\circ)^{-1}$. The arrival time of the *Sp* phase from the Moho is much larger than at the other stations (4.8 s), and its amplitude is much lower (0.09 versus 0.12–0.16). A possible *Sp* phase with negative polarity from the Lehmann discontinuity arrives at a time near −35 s.

For DVP1 we stacked the SRFs from stations MULG (22 functions), MPAD (18 functions) and VARE (15 functions). The average epicentral distance for this data set is 77°. The rms value of noise is 0.008. In the stack there is the *Sp* phase from the Moho at a time of −4.4 s and the $S_{410}p$ phase with a slowness of 0.8 s $(^\circ)^{-1}$ at a time near −55 s. For DVP2, we stacked 27 SRFs with the average distance of 74.3° and the rms value of noise of 0.014. The only signal in this stack is the *Sp* phase from the Moho at a time of −4.2 s.

To summarize, in the first azimuth the $S_{410}p$ phase is present, especially large in the data of HYB and EDC. It is also present in the WDC and DVP. This becomes especially clear when the SRFs from EDC, WDC and DVP are combined into one group (Fig. 13). The $S_{410}p$ phase in the SRFs from the first azimuth is comparable in amplitude with the synthetic amplitude for IASP91 model (Kennett & Engdahl 1991), which indicates that in our SRFs the *S* wave is dominant and the effect of interference between *S* and *SKS* is weak.

The SRFs from the 2nd azimuth do not contain $S_{410}p$. We verify

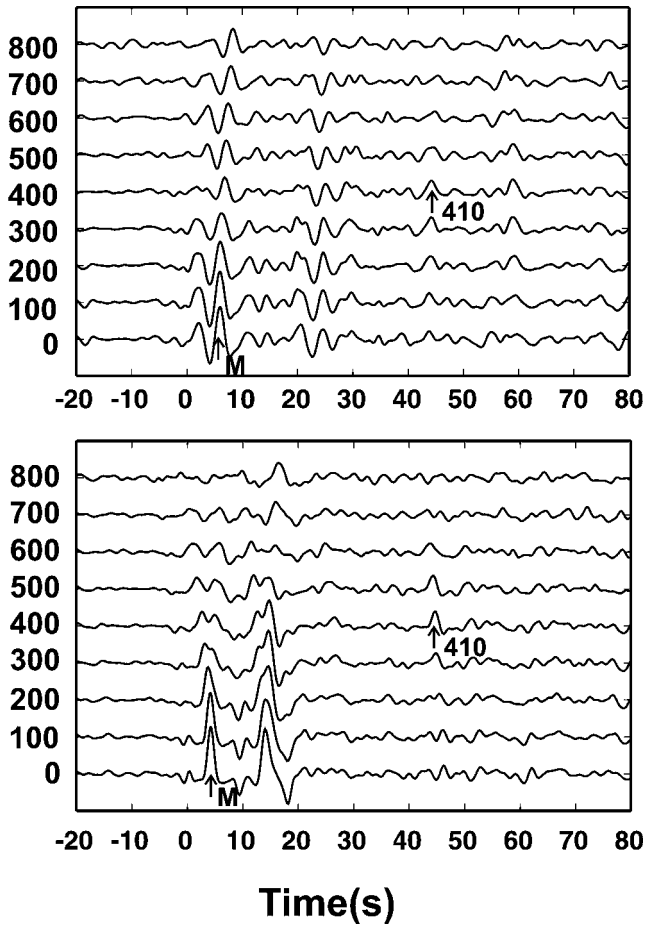

Figure 6. Stacked *Q* components of the *P* receiver functions from stations GRR (top) and GBA + BGL + TMK (bottom). Each trace corresponds to the trial depth in km attached on the left-hand side. Origin of the timescale corresponds to the *P* arrival, but the *P* wave is not seen. Arrivals of the $P_{410}s$ converted phase are labeled 410. *Ps* phases from the Moho are labeled M.

that interference between *S* and *SKS* is not the main reason for this. To check this, we divided HYB2 into two subsets: in a distance range less than 75° and more than 75°, with 35 and 34 individual SRFs, respectively. Interference between *S* and *SKS* is only possible in the 2nd distance range, but we got comparable results for both sub-sets. Observations in the 2nd azimuth are important because they permit us to judge on the magnitude of effects of azimuthal anisotropy—the 2nd azimuth is close to the direction of the Indian plate motion, which may be the fast direction of azimuthal anisotropy, whereas the first direction may be intermediate between the fast and the slow.

Several tens of the PRFs could be obtained for almost every station, and many of them were already shown (Saul *et al.* 2000; Gupta *et al.* 2003; Kumar & Mohan 2005). The differential time between $P_{660}s$ and $P_{410}s$ is always close to the standard 23.9 s (Chevrot *et al.* 1999; Kumar & Mohan 2005), which implies that the discontinuities are at their standard depths. In our study, the recordings required low-pass filtering with a corner period of around 5 s. Low pass filtering permits us, first, to suppress random component of the wavefield and second, to enhance sensitivity of the data to gradational layers. The adopted sign convention for the *P* receiver functions implies positive polarity of the *Ps* phase from positive discontinuity. The examples of the stacked PRFs (Fig. 6) demonstrate clear arrivals of $P_{410}s$ at station GRR from WDC (56 PRFs) and stations EDC (70 PRFs). At GRR, $P_{410}s$ arrives at a time of IASP91 (44.0 s), at EDC it arrives 0.5 s later.

The obtained *S* and *P* receiver functions were inverted jointly. The time interval of the SRFs and PRFs for the inversion was always a few tens of seconds long. This interval usually contains reverberations in the PRFs, which provide useful constraints on the crustal *P* and *S* velocities (Zhu & Kanamory 2000). The trial models consisted of up to 9 layers in the crust and mantle. The layer thickness could be up to several tens of kilometers in the mantle and ∼30 km in the crust. The search was conducted in a broad range of *P* and *S* velocities. The number of the trial models was of the order of 10^5; about 5 per cent of them passed the test.

To invert the receiver functions jointly with the teleseismic traveltime residuals, we assumed that the residuals are accumulated at depths not more than 250–300 km. $P_{410}s$ at stations HYB, WDC and DVP arrives at the standard time of IASP91, and the adopted absolute *P* and *S* traveltime residuals are equal to 0.0 s. Practically similar residuals are observed for HYB1 and HYB2. For EDC the residual of $P_{410}s$ is 0.5 s. Assuming the relationship $dT_S = 2.4\ dT_P$, we obtain $dT_P = 0.4$ s and $dT_S = 0.9$ s.

Observations of $S_{410}p$ at a differential slowness close to the theoretical slowness for the spherically symmetrical Earth imply that the effects of lateral heterogeneity in the crust and mantle of the Dharwar craton are negligible. The models obtained with the traveltime residuals are close to those without the residuals. For HYB1 (Fig. 7) we obtain the crust with a thickness of 31 km and the *S* velocity rising with depth from 3.3 km s^{-1} near the surface to 3.5 km s^{-1} at a depth of 25 km. This layer is underlain by a 6 km thick layer with the *S* velocity of 3.8 km s^{-1}. A similar crustal model is obtained for HYB2 (Fig. 8). Crustal structure of EDC is almost the same, but without the lowermost layer (Fig. 9). Crustal structure of WDC (Fig. 10) is very different—the thickness is 55 km, and the *S* velocity at depths exceeding 15 km is in the mafic range 3.8–4.0 km s^{-1}. This difference is reflected in the anomalous time and amplitude of the *Sp* phase from the Moho. For DVP1 (Fig. 11) crustal thickness is around 35 km; in the upper 20 km *S* velocity is around 3.4 km s^{-1} and in the lower 15 km it is around 3.9 km s^1. A model with the same crustal thickness but a thicker mafic layer is obtained for DVP2 (Fig. 12).

S velocity in the upper mantle (around 4.5 km s^{-1}) beneath all stations is close to that in IASP91. In the *S* velocity profiles for HYB1, WDC and DVP1 there is a small but distinct positive discontinuity in the *S* velocity in the depth interval between 80 and 120 km (80 km for HYB1, 120 km for WDC and 100 km for DVP1). In DVP1, this discontinuity is at the base of a layer with the unusually low *P* and *S* velocities (7.7 and 4.3 km s^{-1}, respectively). This discontinuity is missing in EDC, HYB2 and DVP2. Another noteworthy feature of the models is a low *P* velocity layer between 130 and 170 km depths (HYB1 and EDC), between 190 km and 220 km (HYB2), between160 km and 210 km (WDC) and between 200 km and 240 km (DVP2), sometimes without accompanying variations in the *S* velocity.

4 DISCUSSION AND CONCLUSIONS

Our crustal models are in a good correspondence with geologic data. Beneath the surface exposures of granitoid rocks in the EDC (stations HYB, GBA, TMK, BGL), seismic velocities are in a felsic range; mafic velocities are found only near the Moho boundary in the vicinity of HYB. Surficial amphibolite-grade metamorphic mineral assemblages of the WDC (stations GRR, KSL and TPT)

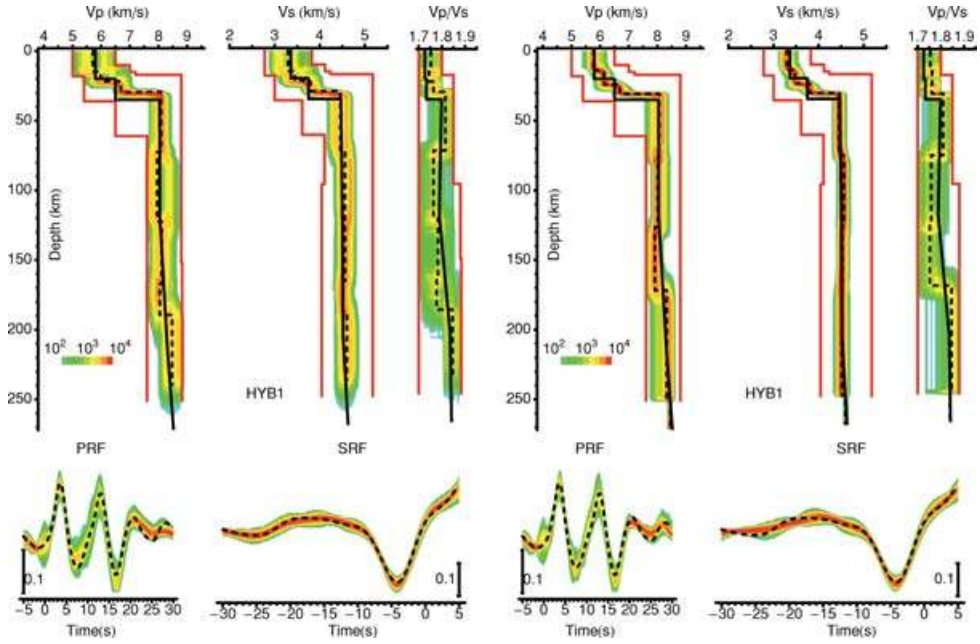

Figure 7. Histograms (colour code) of the velocity models obtained by inversion of the PRFs and SRFs jointly with the *P* and *S* residuals (right-hand side) and without the residuals (left-hand side) for HYB1. Thin red lines show the bounds of the search. IASP91 velocities and their ratios are shown by black lines; dash lines are for the medians. The same colour code shows histograms for the related synthetic components of the PRF and SRF; dash lines are the actual components.

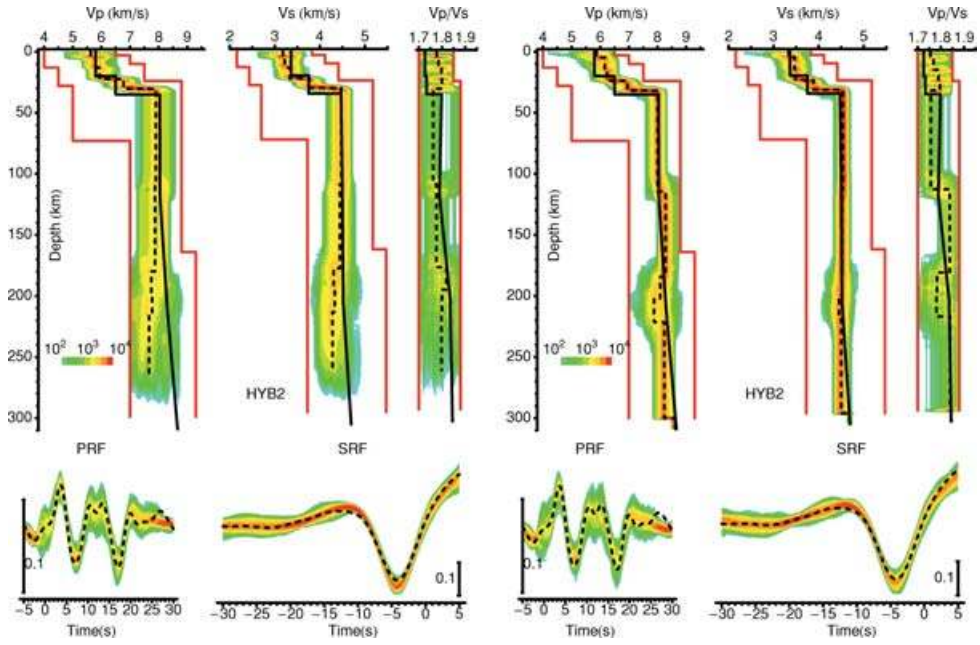

Figure 8. The same as in Fig. 7, but for HYB2.

are underlain at a depth of 10–15 km by the material with seismic velocities in the mafic range. These velocities may correspond to granulites, exposed at the surface in the SGT. Crustal thickness beneath GRR, KSL and TPT (around 55 km) is anomalously large relative to the others stations. Comparable crtustal thickness in this region was reported previously (Gupta *et al.* 2003). This region presents a clear exception to the norm (Durrheim & Mooney 1994), which postulates a thin (27–40 km) crust of felsic composition for the Archean terrains. The crustal models of the DVP are intermediate between the EDC and WDC: the thickness of the crust is close to that of the EDC, but there is a layer with mafic velocities, very thick in DVP2.

The most conspicuous feature of our mantle models is the lack of the high velocity keel, which in other Archean cratons may reach 250–300 km (Jordan 1988). Whereas *S* velocity in the keel is usually around 4.7 km s^{-1} (Grand & Helmberger 1984; Freybourger *et al.* 2001; James *et al.* 2004), the highest velocity in our models is around 4.5 km s^{-1}, similar to IASP91. A very different model, with a high velocity lid and a pronounced low *S* velocity layer (Fig. 12), was obtained for the same region from surface waves

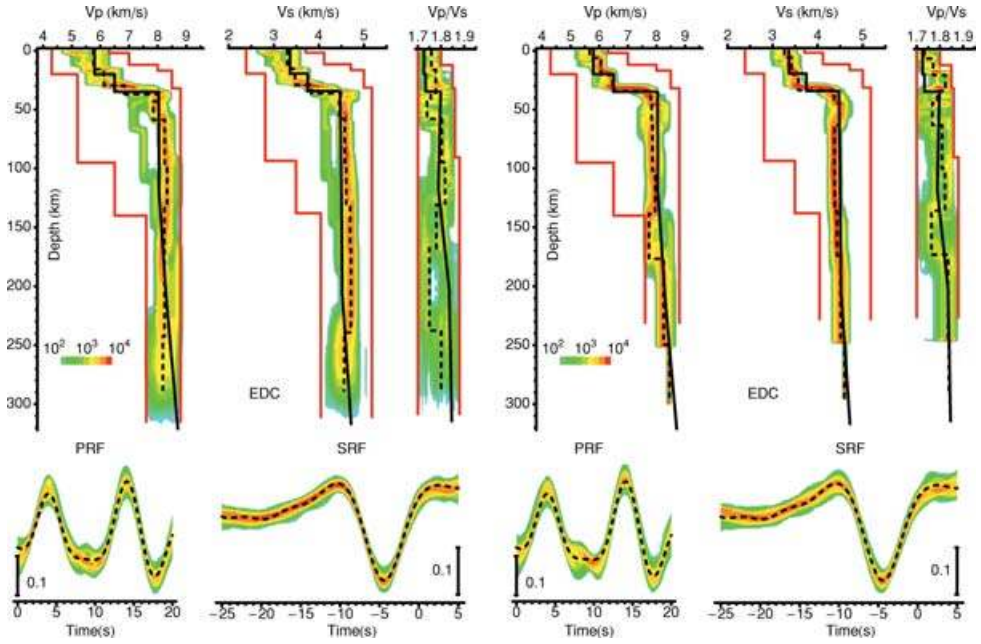

Figure 9. The same as in Fig. 7, but for EDC.

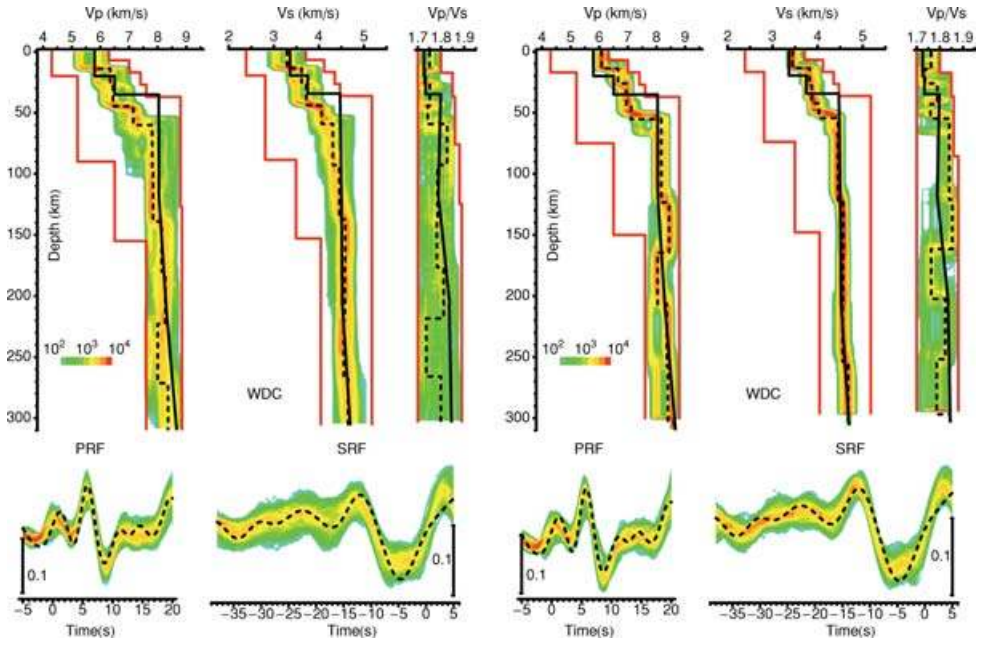

Figure 10. The same as in Fig. 7, but for WDC.

(Mitra *et al.* 2006). To decide, if such models can be reconciled with our data, we stacked the individual SRFs of EDC, WDC and DVP1. In the resulting stack of 150 SRFs (Fig. 13), the rms value of noise is 0.005. The synthetic stack was calculated with the reflectivity techniques for the *S* velocity model of Mitra *et al.* (2006) at depth less than 250 km; at larger depths the adopted model merges with IASP91. *P* velocities were derived from the *S* velocities using their ratio from IASP91 model. Density was found from Birch low. The layer with a negative *S* velocity gradient between 120 and 180 km depths generates in the synthetics the *Sp* phase of positive polarity at a time around −20 s with the amplitude close to that of the *Sp* phase from the Moho. This amplitude is several times the rms amplitude of noise in the stack of the actual SRFs in Fig. 13, but a similar signal in the actual SRFs is certainly missing. The same result was obtained by stacking all available SRFs. Also, *S* velocity in the model of Mitra *et al.* (2006) is at almost any depth higher than in IASP91; it is hard to reconcile this model with the traveltimes of $P_{410}s$ and $P_{660}s$ at our stations, similar to those in IASP91.

The *S* velocity in the uppermost mantle of the Dharwar craton could be reduced by 5 per cent relative to the other cratons by a temperature anomaly of around 300 K (Karato 1993), higher than in most hotspots. A mantle plume beneath the Dharwar craton would generate a pronounced LVZ in the *S* velocities at depths between 100

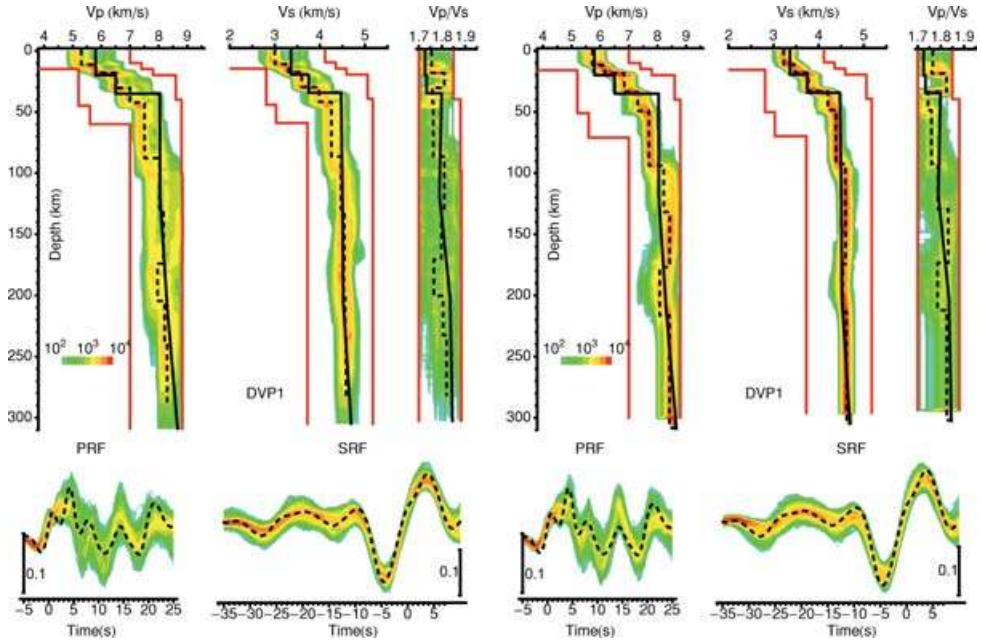

Figure 11. The same as in Fig. 7, but for DVP1.

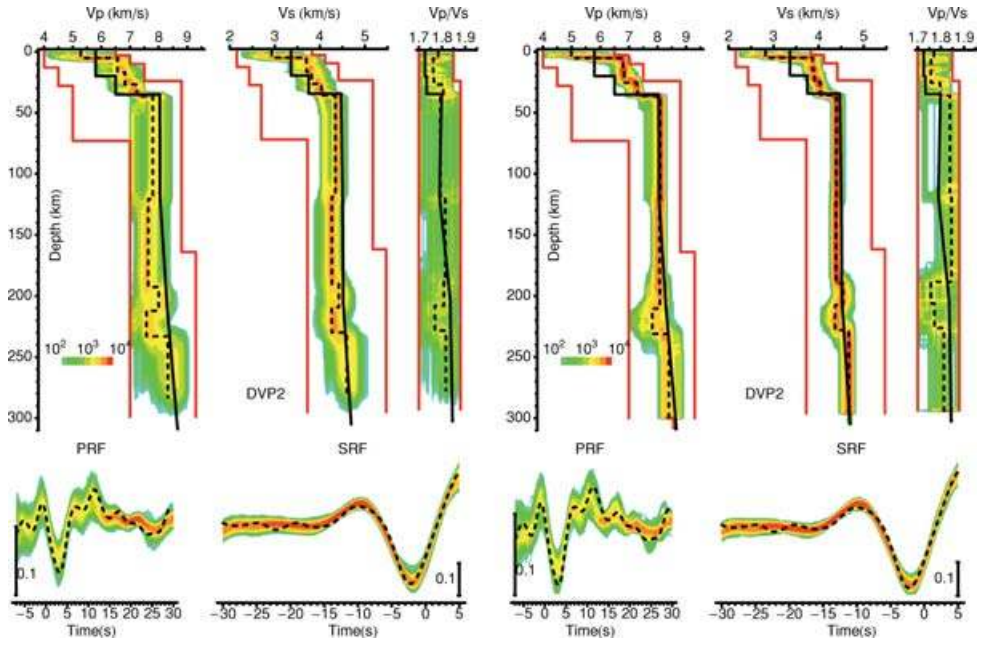

Figure 12. The same as in Fig. 7, but for DVP2.

and 250 km, but such layer is absent. Moreover, any significant heat flow anomaly in south India is unknown (Roy & Rao 2000). These considerations suggest that the low velocity cannot be explained by elevated temperature.

Our best data are obtained from the backazimuth around 100°, and the relatively low *S* velocity might be an effect of azimuthal anisotropy if that is a slow direction in the mantle lithosphere. However, comparable estimates are obtained for the backazimuth around 40°, which, considering the direction of the Indian plate motion, is the likely fast direction. A large azimuthal effect is observed at depths less than 100 km in the DVP, but in the both azimuths the *S* velocity is not higher than 4.5 km s^{-1}. The lack of a large azimuthal effect at HYB is consistent with the indication (Barruol & Hoffmann 1999) that the upper mantle in the vicinity of HYB is isotropic.

Alternative explanation for the low *S* velocity is anomalous composition. To judge on a possible composition of the upper mantle beneath the Dharwar craton, we compare the observed velocities with the properties of mantle xenoliths from the Archean Kaapvaal craton in southern Africa (James *et al.* 2004). These xenoliths, erupted in the last 100 Myr, belong to three groups: (1) spinel lherzolite and harzburgite from the uppermost mantle layer (<100 km); (2) low-temperature garnet lherzolite and harzburgite from depth of 100–180 km and (3) high-temperature garnet lherzolites from depths exceeding 175 km. We compare the *S* velocities, which are

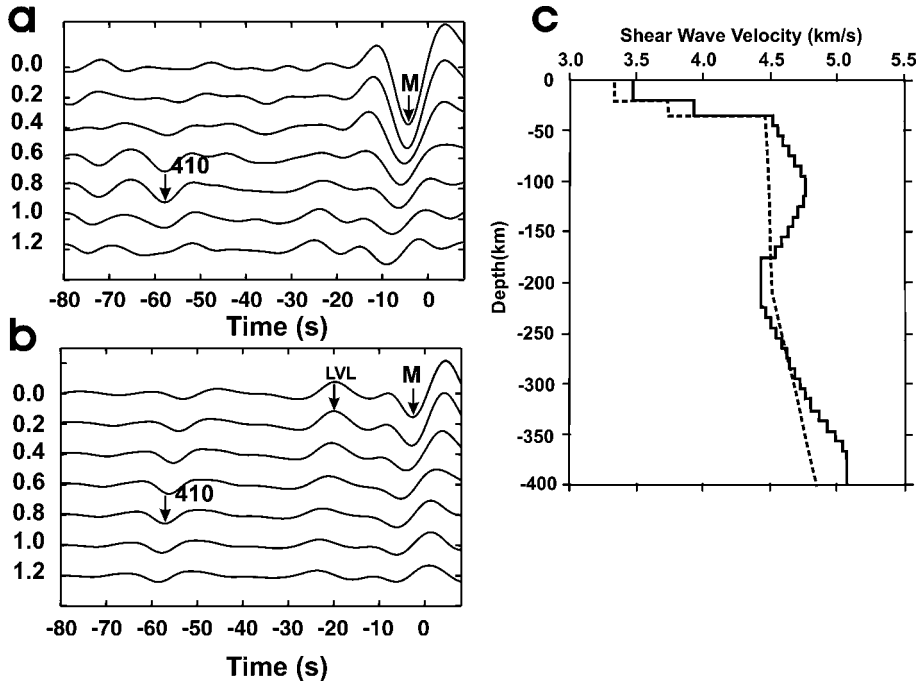

Figure 13. Stacked *L* components of 150 SRFs from EDC, WDC and DVP1 (a) and of the synthetic SRFs (b) for model of Mitra *et al.* (2006) (c). *S* velocity profiles of Mitra *et al.* (2006) and of IASP91 are shown in (c) by solid and dash lines, respectively. The seismic phase labeled LVL in (b) is missing in (a); this is the *Sp* phase from the negative *S* velocity gradient between 120 and 180 km depths in (c).

more accurate than *P*. *S* velocities in the first two groups (around 4.7 km s^{-1}) are very high relative to our models and only in some samples of the third group they are close to 4.5 km s^{-1}. A difference in composition may account for ∼0.15 km s^{-1}—the xenoliths of the third group are 're-fertilized' by metasomatization around the time of eruption, iron enrichment and increase in the proportion of modal clinopyroxene and garnet. A similar process but on a larger scale might reduce the velocities in the uppermost mantle, beneath the the Dharwar craton. Alternatively, the uppermost mantle of the Dharwar craton has never been depleted.

In the best *S* wave profiles (first azimuth, stations HYB, WDC and DVP) we observe a weak positive discontinuity in the depth range from 80 to 120 km. A similar feature (Hales discontinuity) was observed systematically in the *P* wave refraction data in stable continental regions (Hales 1969). The initial explanation of this discontinuity by a transition from spinel peridotite to garnet peridotite is at odds with high pressure data, indicating a much smaller *P* velocity increase at this transition than required by seismic data (James *et al.* 2004). Alternatively, this discontinuity may be an effect of azimuthal anisotropy (Fuchs & Vinnik 1981; Bostock 1998; Levin & Park 2000). A pronounced azimuthal effect in the observations of this discontinuity is seen in the results for the DVP.

Our analysis is less accurate for the *P* velocity and the *P*/*S* velocity ratio. However, we cannot ignore a significant (up to a few percent) reduction in the *P* velocity between 130 and 170 km depths (HYB1 and EDC), between 190 and 220 km (HYB2) and between160 and 210 km (WDC), practically without variations in the *S* velocity. As a result of this, the V_P/V_S velocity ratio in these layers is around 1.75, whereas the normal values are around 1.80.

The decrease in the *P* velocity without a significant effect in the *S* velocity can be explained by the properties of orthopyroxene. *P* velocity of orthopyroxene in the uppermost mantle can be up to 6 per cent lower than of olivine, whereas *S* velocities of both minerals are nearly the same (James *et al.* 2004). The large difference between the *P* velocities of olivine and orthopyroxene may vanish at a depth of 200 km, but the velocities in orthopyroxene appear to be very sensitive to the presence of Al—the bulk modulus increases by about 2 per cent and shear modulus by about 0.7 per cent with every 1 per cent Al .

The low velocity in the fertile lithospheric mantle of the Dharwar craton should be accompanied by high density (Jordan 1988), and if the same composition is preserved in the north of the Indian shield the high density should facilitate subduction of the Indian mantle lithosphere beneath the Himalaya. *P* receiver functions in the northeast of the Indian shield (Ramesh *et al.* 2005) reveal roughly the same crustal thickness and the same arrival times of $P_{410}s$ and $P_{660}s$ as in the Dharwar craton. This similarity implies a similar velocity structure in the upper mantle. A high velocity mantle, different from that beneath the Dharwar craton is found in the northwest of the Indian shield, in the neighbourhood of the western Himalaya (Vinnik *et al.* 2007). Apparently the normal high velocity mantle keel with low density is partially restored there. The variations in density may affect modes of absorption of the mantle lithosphere of the Indian shield along the Himalaya.

Velocities in the upper mantle are high beneath western Tibet relative to the eastern Tibet (Brandon & Romanowicz 1986; Molnar 1990; Dricker & Roecker 2002; Oreshin *et al.* 2008), and this difference can be a direct consequence of the difference in the properties of the subducted mantle lithosphere of the Indian shield in the east and west. The difference in the mantle velocities between the eastern and western Tibet is usually attributed to the difference in temperature, but our analysis suggests the difference in composition of the subducted mantle lithosphere as a possible reason.

ACKNOWLEDGMENTS

The research was supported by Indo-Russian Long Term Program of research cooperation. We are thankful to Vinod Gaur for his help

at several stages of this program. The Russian team was partially supported by the Russian Fund for Basic Research Grant 04-05-64634. We thank the Editor M. Kendall and the anonymous reviewer for their constructive comments.

REFERENCES

Angus, D.A., Wilson, D.C., Sandvol, E. & Ni, J.F., 2006. Lithospheric structure of the Arabian and Eurasian collision zone in eastern Turkey from S-wave receiver functions, *Geophys. J. Int.,* **166,** 1335–1346.

Barruol, G. & Hoffmann, R., 1999. Seismic anisotropy beneath the geoscope stations from SKS splitting, *J. Geophys. Res.,* **104,** 10 757–10 774.

Berkhout, A.J., 1977. Least square inverse filtering and wavelet decomposition, *Geophysics,* **42,** 1369–1383.

Bhattacharya, S.N., 1992. Crustal and upper mantle velocity structure of India from surface wave dispersion, *Curr. Sci.,* **62,** 94–100.

Biswas, N.N., 1972. Earth-flattening procedure for the propagation of Rayleigh wave, *Pure Appl. Geophys.,* **96,** 61–74.

Bostock, M.G., 1998. Mantle stratigraphy and evolution of the Slave province, *J. Geophys. Res.,* **103**(B9), **21** 183–21 200.

Brandon, C. & Romanowicz, B., 1986. A "no-lid" zone in the central Chang-Thang platform of Tibet: evidence from pure path phase velocity measurements of long period Rayleigh waves, *J. Geophys. Res.,* **91,** 6547–6564.

Chevrot, S., Vinnik, L. & Montagner J.-P., 1999. Global scale analysis of the mantle Pds phases, *J. Geophys. Res.,* **104B,** 20 203–20 219.

Dricker, I.G. & Roecker, S.W., 2002. Lateral heterogeneity in the upper mantle beneath the Tibetan plateau and its surroundings from SS-S travel time residuals, *J. Geophys. Res.,* **107**(B11), 2305, doi:10.1029/2001JB000797.

Drury, S.A., Harris, N.B., Holt, R.W., Reeves-Smith, G.J. & Wightman, R.T., 1984. Precambrian tectonics and crustal evolution in south India, *J. Geol.,* **92,** 3–20.

Durrheim, R.J. & Mooney, W.D., 1994. Evolution of the Precambrian lithosphere: seismological and geochemical constraints, *J. Geophys. Res.,* **99**(B8), doi:10.1029/94JB00138.

Farra, V. & Vinnik, L., 2000. Upper mantle stratification by P and S receiver functions, *Geophys. J. Int.,* **141,** 699–712.

Freybourger, M., Gaherty, J.B., Jordan, T.H. & the Kaapvaal Seismic Group, 2001. Structure of the Kaapvaal craton from surface waves, *Geophys. Res. Lett.,* **28**(13), 2489–2492.

Fuchs, K. & Vinnik, L.P., 1981. Investigation of the subcrustal lithosphere and asthenosphere by controlled source seismic experiments on long-range profiles, in *Evolution of the Earth,* pp. 81–98, eds R.J. O'Connell & W.S. Fife, AGU, Washington, DC.

Gaur, V.K. & Priestley, K., 1997. Shear wave velocity structure beneath the Archean granites around Hyderabad, inferred from receiver function analysis, *Proc. Indian Acad. Sci.: Earth Planet. Sci.,* **106,** 1–8.

Grand, S.P. & Helmbereger, D.V., 1984. Upper mantle shear structure of North America, *Geophys. J. R. astr. Soc.,* **76,** 399–438.

Grand, S.P., 2002. Mantle shear-wave tomography and the fate of subducted slabs, *Phil. Trans. R. Soc. Lond.,* **360,** 2475–2491.

Gupta, S., Rai, S.S., Prakasam, K.S., Srinagesh, D., Bansal, B.K., Chadha, R.K., Priestley, K. & Gaur, V.K., 2003. The nature of the crust in southern India—implications for Precambrian crustal evolution, *Geophys. Res. Lett.,* **30**(8), 1419, doi:10.1029/2002GL016770.

Hales, A.L., 1969. A seismic discontinuity in the lithosphere, *Earth Planet. Sci. Lett.,* **7,** 44–46.

Haskell, N.A., 1962. Crustal reflection of plane P and SV waves, *J. Geophys. Res.,* **67,** 4751–4767.

James, D.E., Boyd, F.R., Schutt, D., Bell, D.R. & Carlson, R.W., 2004. Xenolith constraints on seismic velocities in the upper mantle beneath Southern Africa, *Geochem. Geophys. Geosyst.,* **5,** Q01002, doi:10.1029/2003GC000551.

Jordan, T.H., 1988. Structure and formation of the continental tectosphere, *J. Petrol.: Special lithospher issue*, 11–37.

Kaila, K.L. & Krishna, W.G., 1992. Deep seismic sounding in India and major discoveries, *Current Sci.*, Spl. issue: *Seismology in India: an overview,* 62, 117–154, eds H.K. Gupta & S. Ramaseshan.

Karato, S.-I. 1993. Importance of anelasticity in the interpretations of seismic tomography, *Geophys. Res. Lett.,* **20**(15), 1623–1626.

Kennett, B. & Engdahl, E.R., 1991. Travel times for global earthquake location and phase identification, *Geophys. J. Int.,* **105,** 429–465.

Krishna, V.G., 2004. Propagation of regional seismic phases in the Indian shield: constraints on crustal and upper mantle velocity models, *Bull. Seism. Soc. Am.,* **94**(1), 29–43.

Kumar, M.R. & Mohan, G., 2005. Mantle discontinuities beneath the Deccan volcanic province, *Earth Planet. Sci. Lett.,* **237,** 352–263.

Kumar, M.R., Saul, J., Sarkar, D., Kind, R. & Shukla, A., 2001. Crustal structure of the Indian shield: new constraints from teleseismic receiver functions, *Geophys. Res. Lett.,* **28,** 1339–1342.

Levin, V. & Park, J., 2000. Shear zones in the Proterozoic lithosphere of the Arabian shield and the nature of the Hales discontinuity, *Tectonophysics,* **323**(3–4), 131–148.

Metropolis, N., Rosenbluth, M.N., Rosenbluth, A.W., Teller, A.H. & Teller, E., 1953. Equation of state calculations by fast computing machines, *J. Chem. Phys.,* **21,** 1097–1092.

Mitra, S., Priestley, K., Gaur, V.K. & Rai, S.S., 2006. Shear-wave structure of the south Indian lithosphere from Rayleigh wave phase-velocity measurements, *Bull. Seism. Soc. Am.,* **96**(4A), 1551–1559.

Mohan, G., Rai, S.S. & Panza, G.F., 1997. Shear velocity structure of the laterally heterogeneous crust and uppermost mantle beneath the Indian region, *Tectonophysics,* **277,** 259–270.

Molnar, P., 1990. S-wave residuals from earthquakes in the Tibetan region and lateral variations in the upper mantle, *Earth Planet. Sci. Lett.,* **101,** 68–77.

Mosegaard, K. & Vestergaard, P.D., 1991. A simulated annealing approach to seismic model optimization with sparse prior information, *Geophys. Prospect.,* **39,** 599–611.

Mosegaard, K. & Tarantola, A., 1995. Monte Carlo sampling of solutions to inverse problems, *J. Geophys. Res.,* **100**(B7), 12 431–12 447.

Negi, J.G., Pandey, O.P. & Agrawal P.K., 1986. Super-mobility of hot Indian lithosphere, *Tectonophysics,* **131,** 147–156.

Oreshin, S., Kiselev, S., Vinnik, L., Prakasam, S., Rai, S.S., Makeyeva, L. & Savvin, Y., 2008. Crust and mantle beneath western Himalaya, Ladakh and western Tibet from integrated seismic data, *Earth Planet. Sci. Lett.,* in press.

Raase, P., Raith, M.M., Ackermond, D. & Lal, R.K., 1986. Progressivbe methamorphism of mafic rocks from greenschist to granulite facies in the Dharwar craton of south India, *J. Geol.,* **94,** 261–182.

Rai, S.S., Priestley, K., Suryaprakasam, K., Srinagesh, D., Gaur, V.K. & Du, Z., 2003. Crustal shear velocity structure of the south Indian shield, *J. Geophys. Res.,* **108,** 2088, doi:10.1029/2002JB001776.

Ramesh, D.S., Kumar, M.R., Devi, E.U. & Raju, P.S., 2005. Moho geometry and upper mantle images of northeast India, *Geophys. Res. Lett.,* **32,** L14301, doi:10.1029/2005GL022789.

Roy, S. & Rao, R., 2000. Heat flow in the Indian shield, *J. Geophys. Res.,* **105,** 25 587–25 604.

Sarkar, D.K., Chandrakala, P., Devi, P.P., Sridhar, A.R., Sain, K. & Reddy, P.R., 2001. Crustal velocity structure of western Dharwar craton, South India, *J. Geodyn.,* **31,** 227–241.

Saul, J., Kumar, M.R. & Sarkar, D., 2000. Lithospheric and upper mantle structure of the Indian shield, from teleseismic receiver functions, *Geophys. Res. Lett.,* **27**(16), 2357–2360.

Taylor, P.N., Moorbath, S., Chadwick, B. Ramakrishnan, M. & Vishwanatha, M.N., 1984. Petrography, Chemistry and isotopic ages of peninsular gneiss, Dharwar acid volcanic, Precambrian Research, **23,** 349–375

Vinnik, L., 1977. Detection of waves converted from P to SV in the mantle, *Phys. Earth Planet. Inter.,* **15,** 39–45.

Vinnik, L.P., Chevrot, S., Montagner, J.-P. & Guyot, F., 1999. Teleseismic travel time residuals in North America and anelasticity of the asthenosphere, *Phys. Earth Planet. Inter.,* **116,** 93–103.

Vinnik, L.P., Reigber, Ch., Aleshin, I.M., Kosarev, G.L., Kaban, M.K., Oreshin, S.I. & Roecker, S.W., 2004. Receiver function tomography of the central Tien Shan, *Earth Planet. Sci. Lett.,* **225,** 131–146.

Vinnik, L.P., Aleshin, I.M., Kaban, M.K., Kiselev, S.G., Kosarev, G.L., Oreshin, S.I. & Reigber, Ch., 2006. Crust and mantle of the Tien Shan from the data of the receiver function tomography, *Izvestia, Phys. Solid Earth,* **42,** 639–651.

Vinnik, L., Singh, A., Kiselev, S. & Kumar, M.R., 2007. Upper mantle beneath foothills of the western Himalaya: subducted lithospheric slab or a keel of the Indian shield? *Geophys. J. Int.,* **171,** 1162–1171.

Wilson, D.C., Angus, D.A., Ni, J. & Grand, S., 2006. Constraints on the interpretation of S-to-P receiver finctions, *Geophys. J. Int.,* **165,** 969–980.

Zhu, L. & Kanamori, H., 2000. Moho depth variation in southern California from teleseismic receiver functions, *J. Geophys. Res.,* **105,** 2969–2980.

Zhou, L., Chen, W.-*P*. & Ozalaybey, S., 2000. Seismic properties of the Central Indian shield, *Bull. Seism. Soc. Am.,* **90,** 1295–1304.